PHYSICAL REVIEW E **80**, 036307 (2009)

Pore-network extraction from micro-computerized-tomography images

Hu Dong[*] and Martin J. Blunt
Department of Earth Science and Engineering, Imperial College London, London SW7 2AZ, United Kingdom

(Received 8 October 2008; revised manuscript received 1 June 2009; published 14 September 2009)

Network models that represent the void space of a rock by a lattice of pores connected by throats can predict relative permeability once the pore geometry and wettability are known. Micro-computerized-tomography scanning provides a three-dimensional image of the pore space. However, these images cannot be directly input into network models. In this paper a modified maximal ball algorithm, extending the work of Silin and Patzek [D. Silin and T. Patzek, Physica A **371**, 336 (2006)], is developed to extract simplified networks of pores and throats with parametrized geometry and interconnectivity from images of the pore space. The parameters of the pore networks, such as coordination number, and pore and throat size distributions are computed and compared to benchmark data from networks extracted by other methods, experimental data, and direct computation of permeability and formation factor on the underlying images. Good agreement is reached in most cases allowing networks derived from a wide variety of rock types to be used for predictive modeling.

DOI: 10.1103/PhysRevE.80.036307 PACS number(s): 47.56.+r, 47.61.Jd, 87.57.N−

I. INTRODUCTION

Pore-scale modeling has been widely used as a platform to study multiphase flow in petroleum engineering, hydrology, and environment engineering [1–3]. The pore space in a rock is represented by a network of pores (corresponding to the larger void spaces) and throats (the narrow openings connecting the pores) with parametrized geometries and topology through which multiphase flow can be simulated. However, this network, to be representative of the porous medium of interest, should be derived directly from an analysis of the pore-space geometry.

There are three ways in which a three-dimensional (3D) representation of the pore space can be obtained. The first is through direct imaging, usually by micro-x-ray computerized tomography (micro-CT) [4,5]. Micro-CT allows samples a few millimeters across to be imaged nondestructively at a resolution of a few microns or submicron using nano-CT scanners [4]. This method is suitable to image microstructures of a wide range of sandstone and carbonate rocks. The second approach is to use a statistical model to generate synthetic 3D structures that capture the properties of two-dimensional (2D) thin sections, which are routinely available at a sufficiently high resolution to capture the microstructure of hydrocarbon-bearing rocks [6–14]. To reproduce the connectivity and shapes of the pore structures, several reconstruction approaches have been recently proposed, for instance, the multiple-point method [15] or the five-point stencil method using a Markov chain Monte Carlo model [16], which reproduce typical patterns of the void space seen in 2D and consequently preserves the long-range connectivity. These statistical methods produce high resolution 3D images derived from their original 2D inputs with similar morphological statistics. The third method is to simulate the packing of grains followed by the geological processes such as sedimentation, compaction, and digenesis by which sedimentary structures were formed. This method was pioneered by Bryant and co-workers [17–19] and later extended by Øren and Bakke [20–22]. The simulated rock images produce good agreement with micro-CT images of Fontainebleau and Berea sandstone in terms of morphological properties, such as two-point correlation functions, local porosity distributions and local percolation probabilities, and petrophysical properties such as absolute permeability and formation factor [20–22].

While it is possible to simulate single-phase flow directly in 3D pore-scale images [23,24], to date most success in predicting capillary-controlled multiphase flow has been achieved using network models, where the details of the pore space are replaced by an equivalent network of pores and throats [20–23,25–28]. So far these networks have been extracted using process-based methods; since, by construction, the grain centers are known, an ultimate dilation of the grains can be performed to tessellate the pore space using Voronoi polyhedra [17–22]. Although these process-based models are able to generate representative pore structures when the sedimentary processes can be simulated, to widen the range of samples for which predictions of multiphase properties may be made, it is necessary to develop a network extraction technique that can be generally applied to any 3D image of interest. This is particularly important for carbonates that typically have a very complex sedimentary and diagenetic history that is not easy to be reproduced using a process-based model.

Attempts to extract pore networks from generic and arbitrary 3D images have been tried for more than a decade. The major algorithms include the medial axis based method and the maximal ball (MB) method. The former transforms the pore space into a medial axis that is the reduced representation of the pore space acting as a topological skeleton roughly running along the middle of pore channels either by a thinning algorithm [29,30] or a pore-space burning algorithm [31]. Pore-space partitioning can be validated along the skeleton to decide the pore throats by local minima along branches and pore bodies at the nodes [31–35]. The medial axis mathematically preserves the topology of the pore space. However, it is difficult to identify pores unambigu-

---

[*] Present address: Numerical Rocks AS, Stiklestadveien 1, N-7041 Trondheim, Norway.

ously. Clean-up processes need to be performed to remove trifling details on the skeleton due to the intrinsic sensitivity of the algorithm to noise in digitalized images [32], especially to that in the form of the bumps on the surface [33]. Furthermore, pores normally encompass more than one junction of the medial axis; therefore, various merging algorithms have to be developed to trim the skeleton and fuse the junctions together while avoiding unrealistically high coordination numbers (the number of independent throats linked to a pore) [33,35,36].

The maximal ball algorithm [37–39] finds the largest inscribed spheres centered on each voxel of the image that just touch the grain or the boundary. Then those included in other spheres are viewed as inclusions and removed; the rest are called maximal balls and describe the pore space without redundancy. Locally the largest maximal balls identify pores while the smallest balls between pores are throats. Maximal balls were used by Silin *et al.* [38,39] to find the dimensionless capillary pressure in drainage. Al-Kharusi and Blunt [37] extended this method and developed a more comprehensive set of criteria to determine the maximal ball hierarchy including sphere clusters to handle equally sized balls. However, Al-Kharusi and Blunt's algorithm uses a tremendous amount of computer memory and time and consequently was limited to relatively small systems containing fewer than a thousand pores. Moreover, their method tends to form pores with very high coordination numbers.

II. NETWORK EXTRACTION ALGORITHM

We used Silin and Patzek's maximal ball concept [38,39] to develop an efficient algorithm to extract pore networks. The major differences of this work from Silin and Patzek's and Al-Kharusi and Blunt's [37] are as follows: (i) we developed a two-step searching algorithm to find the nearest solid to define a void ball instead of growing a ball layer by layer; (ii) we invented a clustering process to define pores and throats by affiliating the maximal balls into family trees according to their size and rank.

A. Building maximal balls

MBs are the basic elements used in our method to define the pore space and detect the geometrical variations and connectivity. As a set of voxels assembling a largest sphere, a MB must touch the grain surface; every MB must be in possession of at least one voxel that is not contained in any other MB. Accordingly, we first build an inscribed sphere at each void voxel, and then remove those included in others.

To build spheres inscribed to the grain or image boundary, we designed a two-step searching algorithm. Instead of attaching void voxels, assembling a ball until it hits a grain or boundary, we use an *inflating search* to define the potential search range followed by a *deflating search* to find the genuine nearest solid voxel to define the radius. During the *inflation* step, we search for solid or boundary voxels along 26 directional lines (6 lateral, 12 diagonal, and 8 diametrical lines). The stop point defines the range for the *deflating searching* where *all* voxels (including the undetected along the 26 investigated directions) contained within the range are checked to find the genuine nearest solid voxel.

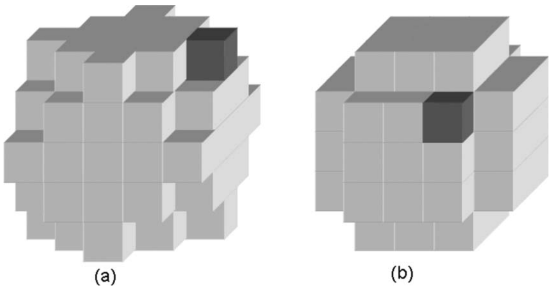

FIG. 1. Illustration of radius definition. (a) A digital sphere with a radius of $\sqrt{8}$ to define R_{RIGHT}; (b) a digital sphere with a radius of $\sqrt{6}$ to define R_{LEFT}.

We introduce the lower and upper limits as a range to indicate the sphere size instead of a single radius, since it is difficult to give a precise single value to the radius due to the discontinuity caused by individuality of voxels in a discrete 3D image. The upper limit (denoted by R_{RIGHT}) is defined by the Euclidean distance from the center to the nearest grain voxel found by the two-step searching; the lower limit (denoted by R_{LEFT}) is defined by the center of the farthest void voxel from the center within the sphere defined by R_{RIGHT}. We define them squared in the algorithm, i.e., $R^2_{LEFT} \le R^2 < R^2_{RIGHT}$. R is the real radius of the ball. Both R^2_{LEFT} and R^2_{RIGHT} must be the sums of three square numbers.

Figure 1 provides an example to illustrate how the radius is defined. If the nearest solid to the center is the dark voxel shown in Fig. 1(a), this defines R^2_{RIGHT} ($R^2_{RIGHT}=0^2+2^2+2^2=8$); the farthest void voxel is the dark voxel in Fig. 1(b) to define R^2_{LEFT} ($R^2_{LEFT}=1^2+1^2+2^2=6$). The actual MB has a radius square between R^2_{LEFT} and R^2_{RIGHT}.

We use C_A and C_B to denote the centers of two balls A and B; dist(C_A,C_B) is the distance between the two centers. If dist$(C_A,C_B) \le (R_{RIGHT\ A} - R_{LEFT\ B})$, we remove ball B as an inclusion. The compound (R_{LEFT} and R_{RIGHT}) provides more accuracy for the inclusion removal; see an example in Fig. 2. After the inclusions are removed, the remaining balls are called maximal balls and describe the pore space without redundancy.

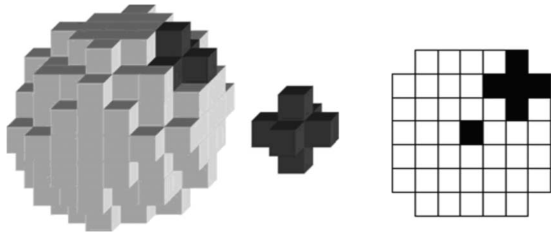

FIG. 2. The R_{LEFT} of the larger ball on the left is $\sqrt{13}$ voxel lengths. The R_{RIGHT} of the middle smaller ball is 1. The right picture shows the central cross section of the balls put together. The small ball is clearly included in the larger one. However, the condition dist$(C_A,C_B) \le (R_{LEFT\ A} - R_{LEFT\ B})$ cannot detect the inclusion. The difference of their R_{LEFT}s is $\sqrt{13}-1$, which is smaller than the distance $\sqrt{8}$ between the centers. Using R_{RIGHT} for the outer ball radius can overcome this problem.

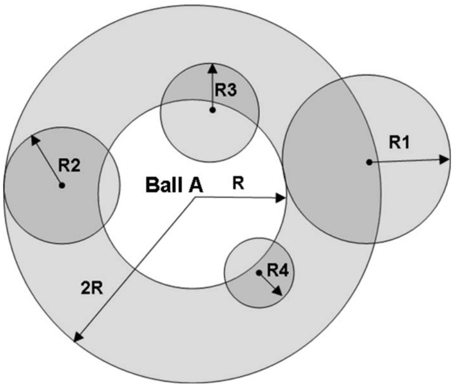

FIG. 3. Schematic of ball A absorbing all its overlapping neighbors who are not bigger than A ($R \geq R_1 \geq R_2 \geq R_3 \geq R_4$). Since we start the absorption from big pores, the $2 \times R$ radial range is sufficient to accommodate all the ball centers of its smaller or same sized neighbors.

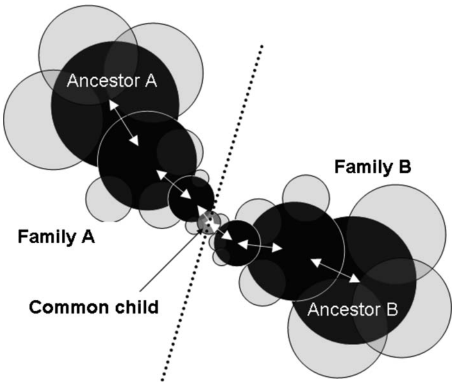

FIG. 4. Schematic of two families A and B, the ancestors of the two families, their common child defining the throat and the pore-throat chains along white arrows. The black balls are on the pore-throat chains (white arrows) along the skeleton; the light balls are pore bodies that are not on the skeleton but describe the pore space.

B. Clustering the maximal balls

We invent a clustering process to organize the maximal balls into pore-throat chains by following the procedure below:

(1) We sort all the MBs from the largest to the smallest and then divide them into subsections according to size. Each group contains MBs of the same size. Let M denote the number of MBs in the first group representing the largest balls. All the MBs are initially given infinite rank.

(2) Starting from the first ball A in the image with the largest radius, we define it as a pore and rank it first as an ancestor. All its smaller (or same sized) overlapping neighbors are absorbed by A and ranked second generation shown in Fig. 3. Every ball in this cluster remembers that A is its ancestor and parent.

(3) We collect the same sized balls left in the first group and sort these M-1 balls by their rank. Starting from the first, ball B absorbs its smaller unranked neighbors and ranks them one generation younger. The clustered balls inherit the family name of ancestor and know B as parent. If B's rank was infinite before being processed, B defines a new pore as an ancestor (e.g., the ancestor A or B in Fig. 4). If not, B is regarded as part of its ancestor's pore body and ready to transfer the family name to its offspring (e.g., other black balls in Fig. 4). If B absorbs any MBs from two families, B's common child defines a throat (e.g., the common child in Fig. 4). Once a throat is found, a pair of pore-throat chains (the white arrows in Fig. 4) is constructed from the throat to ancestors by visiting parents layer upon layer.

(4) The same sorting and clustering processes apply for the next MB that has the same size. After all the balls in this group are processed, we move to the next group with a smaller size.

(5) The same sorting and clustering processes apply for all the groups until we reach the minimum size set for a pore. Below this threshold, we only allow MBs to provide connections but not to be pores.

C. Pore-space segmentation and parameter calculations

After the clustering, pore-throat chains are constructed throughout the pore space as bundled skeletons. However, there might be one or more pore-throat chains winding through the void space between pores, if there are more common children defined during clustering between two family trees. These parallel links will be merged in later steps. The remaining MBs can be associated to the chains as flesh to describe the profiles of the pore space using the parenting hierarchy established during clustering. We then segment the pore space into pores and throats according to these chains. What is a pore and what constitutes a throat is somewhat arbitrary; in topological terms all we need to assign is the connectivity of the void space. However, how we divide the void space into pores and throats has an impact on the prediction of transport properties. For example, the sizes and lengths of the pores and throats affect computation of permeability and the volumes of elements have effects on the saturation calculation. The pore-space segmentation has to be optimized by benchmarking against the reference data, as will be described later.

We initially set the border between a pore and a throat along the chain where a MB can be found having a radius of 0.7 times the ancestor's radius. If there is another link parallel to this, we move the border to where the two links intersect and merge the two. Voxels are assigned uniquely to either the pore or the throat according to the eventual border of the pore throat. Consequently, the pore space is divided into pore blocks and throat blocks. The method gives the same coordination number consistently to each pore regardless of this pore and throat segmentation.

Parameters associated with pores and throats are calculated to extract the full network as the input to the two-phase flow simulator developed by Valvantne and Blunt [26]. The sizes of pores and throats are assigned randomly between $(R_{LEFT}-1)$ and R_{RIGHT}; additionally, the minimum size is set to 0.1 times the voxel side length. The smoothing is to reduce the discreteness on size distributions. The volume is calculated by counting the number of void voxels in each block of a pore or throat. The length of the element is defined similarly to that given by Øren and Bakke [21]; see Fig. 5.

The throat length l_t is defined by subtracting the two pore lengths l_i and l_j (the Euclidean distance from pore center to

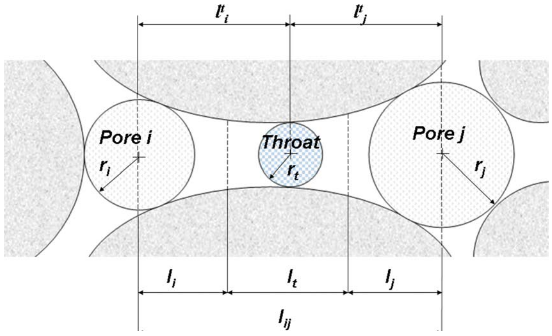

FIG. 5. (Color online) Schematic of the length definition for pores and throats.

pore-throat border) from the throat total length l_{ij} (the Euclidean distance from pore i center to pore j center),

$$l_t = l_{ij} - l_i - l_j. \tag{1}$$

The pore lengths l_i and l_j are defined by

$$l_i = l^t_i \left(1 - \alpha \frac{r_t}{r_i}\right), \tag{2}$$

$$l_j = l^t_j \left(1 - \alpha \frac{r_t}{r_j}\right), \tag{3}$$

where r_i, r_j, and r_t are the radii of *pore* i, *pore* j, and *throat*, respectively; l^t_i and l^t_j are the Euclidean distances between the centers of pore i and pore j to the throat center; α is the pore-throat segmentation coefficient to decide the pore-throat interface along the pore channels. Øren and Bakke [21] used 0.5 for this coefficient for network construction, by which the pore channel can be equally divided into pore and throat when they have the same radii. We use 0.6 as the segmentation coefficient in this study, by which we tend to define longer throats than Øren and Bakke's. This value is determined by calibrating the network permeability with lattice Boltzmann simulation results (in Table III). The pore and throat lengths in our networks are defined using Euclidean distances; we ignore the tortuosity along the predefined pore-throat chains.

Real pores and throats have complex and high irregular geometrical profiles. We approximate them as cylindrical capillaries with a constant but arbitrary cross section with a dimensionless shape factor G,

$$G = \frac{VL}{A_s^2}, \tag{4}$$

where A_s is the surface area of the pore or throat block—this is found by counting the number of surface voxels of each block; V is block volume and L is the block length defined as twice the Euclidean distance between the ancestor ball's center to the farthest voxel in its block. This is an equivalent to

$$G = \frac{A}{P^2}, \tag{5}$$

where A is the cross-sectional area and P is perimeter [40].

III. DATASETS

A. Simple sphere packings

Five 3D images of regular packings of equally sized spheres were provided by Øren and Bakke [20–22] using the process-based method (denoted by PB). The packings are cubic, orthorhombic, tetragonal-sphenoidal, rhombohedral-pyramidal, and rhombohedral-hexagonal packs named according to the center arrangement. In these packs, each sphere has a diameter of 50 times the voxel length. Each image consists of 120^3 voxels and contains fewer than a hundred pores. These images were used to compare the number of pores defined by PB and MB methods.

B. Fontainebleau sandstone

Fontainebleau sandstone is an ideal granular system consisting of monocrystalline quartz grains that have been well rounded through transport for long periods before being deposited [41]. This sandstone has a grain size around 250 μm and contains no clay. The porosity varies from 2% to 30% depending on the degree of compaction and diagenesis without noticeable grain size modification [15]. In this study, we used a PB reconstructed image (Fig. 6, top) of Fontainebleau sandstone [20] with a porosity of 13.6% consisting of 300^3 voxels across a volume of 11.39 mm^3 to extract the MB network to compare with the PB network.

C. Berea sandstone

Berea sandstone is another standard material consisting of quartz with minor amounts of feldspar, dolomite, and clays, which is also widely used for core analysis [42–44] due to its fine-grained, well-sorted characteristics with closely spaced planar bedding [15]. A Berea sandstone was imaged at Imperial College using a phoenix v|tome|x micro-CT system with a resolution (voxel edge size) of 5.345 μm (Fig. 6, bottom). A subsection consisting of 400^3 voxels representing 9.8 mm^3 with a porosity of 19.6% is used in this study to extract a pore network to compare the structure and transport properties against the results of a PB pore network of Berea sandstone [21] and the multiphase flow experiments with a water-wet Berea sandstone performed by Oak [42].

D. Other samples

A series of rock samples has been selected and micro-CT imaged [45]. The network extraction algorithm was tested on these 12 samples. The networks were extracted to calculate porosity, absolute permeability, and formation factors.

The micro-CT scanner outputs a 3D image which is a 3D array of gray scales. The gray scales are then segmented to define pore space and rock matrix. To enhance the contrast between void and grain and remove the noise, a median filter [46] was applied to the images before choosing a threshold value to binarize the gray scales into black (void) and white (solid). These micro-CT images are part of our image library which will accommodate a wide range of sandstone and carbonate micro-CT images in the future. This work has two aims. One is to carry on extensive study on pore-space im-

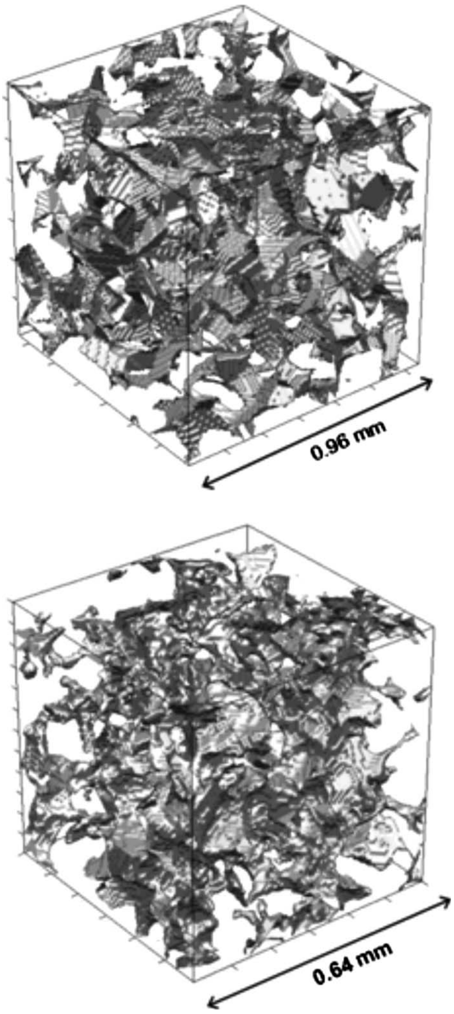

FIG. 6. 3D view of subsamples of the reconstructed Fontainebleau (top) and Berea (bottom) micro-CT images used in this study.

ages and the derived networks to work out a comprehensive set of criteria to determine scanning parameters such as sample size, resolution, representative elementary volume, and the proper filtering and thresholding values for the image processing. The other aim is that after the completion of this library, to predict the transport properties for new samples, we only need to find the samples in the library with similar structures and do some minor change to the network parameters, such as pore sizes, throat sizes, aspect ratio, and porosity for predictions—see examples in [26].

IV. RESULTS

A. Comparison on pore network structures

Pore networks are extracted from the 3D images of sphere packings, Fontainebleau and Berea sandstone. We compare the MB pore network structures to PB networks in terms of numbers of elements and their connectivity, size distributions, volumes, lengths, shape factors, and aspect ratios.

1. Regular sphere packings

We compare the number of pores defined by the two methods. Since the two methods consider boundaries differently, we compare the interior pores. For the studied packings, the two methods found 8, 16, 86, 36, and 42 interior pores in cubic, orthorhombic, tetragonal-sphenoidal, rhombohedral-pyramidal, and rhombohedral-hexagonal packings, respectively. In all cases both methods gave results identical to the analytical predictions.

TABLE I. Number of pores and throats defined in Fontainebleau and Berea sandstone networks.

	Fontainebleau network		Berea network	
Number of elements	PB	MB	PB	MB
No. of pores	4997	3101	12349	6298
No. of throats	8192	6112	26146	12545
No. of boundary pores	433	289	433	447

2. Fontainebleau and Berea sandstone

The MB method defines fewer pores than the PB approach for the reconstructed Fontainebleau sandstone, for both interior and boundary regions (see Table I), which indicates that the two methods have different criteria to treat boundaries and to merge pores. The Berea networks were extracted from two images with different sizes and resolutions. The MB method defines more pores per unit volume ($644\ \text{pores/mm}^3$) than in the PB network ($457\ \text{pores/mm}^3$). This could be because the voxel size of the micro-CT image is finer than for the PB image and the grain size in the PB image could be coarser. As we will show later, the latter explanation—a larger grain size—is more likely. Nevertheless, our methods should be independent of image resolution as long as all the relevant pore-space features are captured. The discrepancy is not significant as long as the pore network is able to capture the topology of pore space and predict transport properties accurately.

The topology (or connectivity) of the pore network is quantitatively expressed by coordination numbers. For Fontainebleau networks, the average coordination numbers of MB network is 3.85 while it is 3.19 for the PB network. The maximum coordination numbers are 12 for the former and 10 for the latter. The coordination number distributions are similar, Fig. 7, except that the MB network defines more pores with higher coordination numbers. For Berea networks, the average coordination numbers are similar although the peak values are different. More pores with both low (0, 1, and 2) and high (more than 10) coordination numbers are found in the MB network. The reason is that the MB network derived from a micro-CT image with a higher noise level (compared to the reconstructed image) is more likely to find smaller satellite pores (sometimes only artifacts due to imaging) around big pores.

Figures 8 and 9 show the distributions of inscribed radii of pores and throats of these networks. Good agreement is obtained between the pore size distributions of MB and PB networks for both samples, even though the MB network has a slightly wider distribution than for the PB method for the Fontainebleau sample. The MB method finds throats which

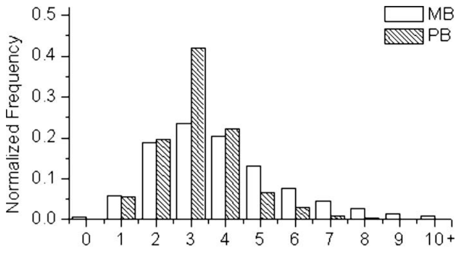

(a) Coordination Number

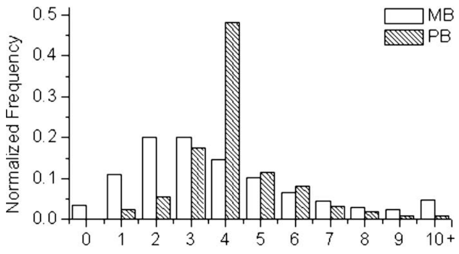

(b) Coordination Number

FIG. 7. Coordination number distributions of MB and PB networks of (a) Fontainebleau networks and (b) Berea networks.

are smaller than in PB networks for both samples, which is consistent with the earlier observation that large elements identified as “throats” by the PB method are merged into pore bodies in the MB method.

Figure 10 shows the distribution of pore and throat volumes for Fontainebleau sandstone. Since fewer pores and throats are found in the MB network than in the PB method, one would expect both pore and throat volumes to be larger. While this is the case for pores, the throat volumes are similar, which suggests that the MB method tends to underestimate the throat size. The Berea networks show similar pore volume distributions (Fig. 11) for the two networks.

The pore spacing (distance between two adjacent pore centers) distributions are compared in Fig. 12. It is found that the MB method tends to define longer connections than the PB method. This is because of the merging of what would be pores in the PB method, giving fewer, larger pores in the MB network.

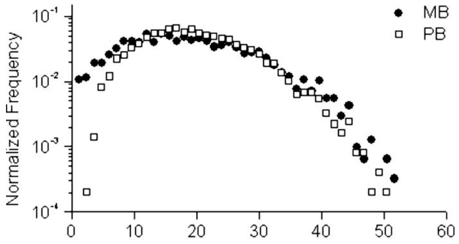

(a) Pore Radius (μm)

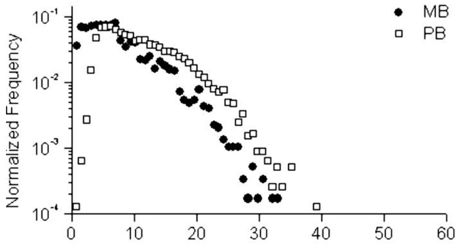

(b) Throat Radius (μm)

FIG. 8. Distributions of (a) pore sizes and (b) throat sizes for Fontainebleau networks.

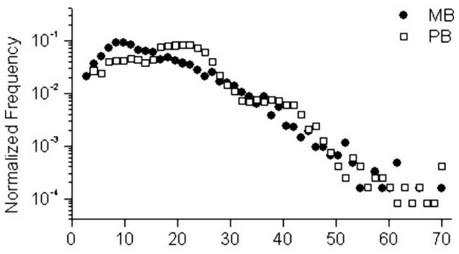

(a) Pore Radius (μm)

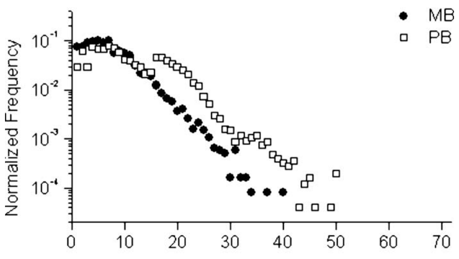

(b) Throat Radius (μm)

FIG. 9. Distributions of (a) pore sizes and (b) throat sizes for Berea networks.

The aspect ratio is the ratio of pore radius to the linked throat radius. The aspect ratio distributions are compared in Fig. 13. The two methods give similar distributions of the aspect ratios; even though, MB defines slightly higher aspect ratio than the PB method since it allows some very small throat radii.

In the pore shape factor distributions (Fig. 14), a left-side offset can be found in the MB networks compared to the PB ones, which means a higher order of shape irregularity is defined for MB elements. For the pores whose shape factors are computed, the distribution is consistent with the fact that

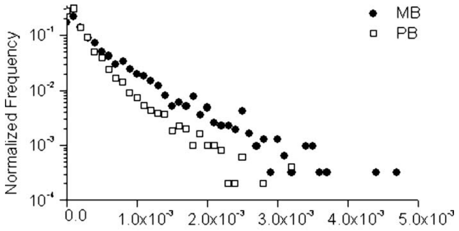

(a) Pore Volume (mm^3)

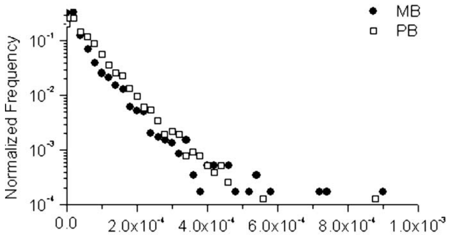

(b) Throat Volume (mm^3)

FIG. 10. Distributions of (a) pore and (b) throat volumes for Fontainebleau networks.

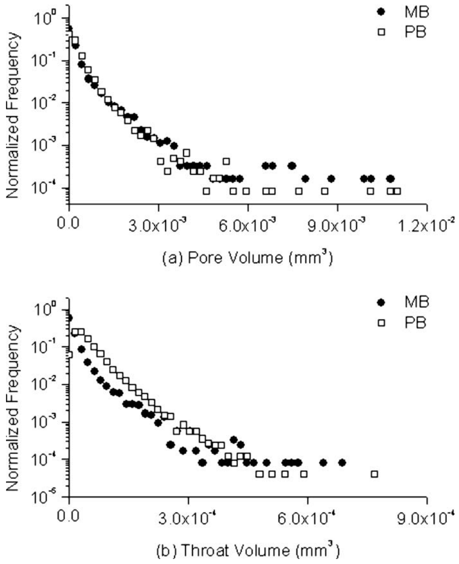

FIG. 11. Distributions of (a) pore and (b) throat volumes for Berea networks.

the MB method tends to have fewer pores while accounting for the same pore/grain surface area.

B. Single-phase flow properties

To assess the quality of the network extraction, we applied the simulator (available online http://www3.imperial.ac.uk/earthscienceandengineering/research/perm/porescalemodelling/software/two%20phase%20code) developed by Valvatne and Blunt [26] to predict single- and two-phase flow. We do not distinguish the clay content in any of the images. However, to match the irreducible water saturation observed in Oak's experiment [42] for Berea sandstone, we distribute clay uniformly to each element of the Berea MB network—this clay remains water-filled. The absolute permeability and formation factors calculated on the networks are compared to the results computed directly on the voxelized micro-CT images using the lattice Boltzmann method for absolute permeability [23,24] and solving the Laplace equation on the images for the formation factor [20].

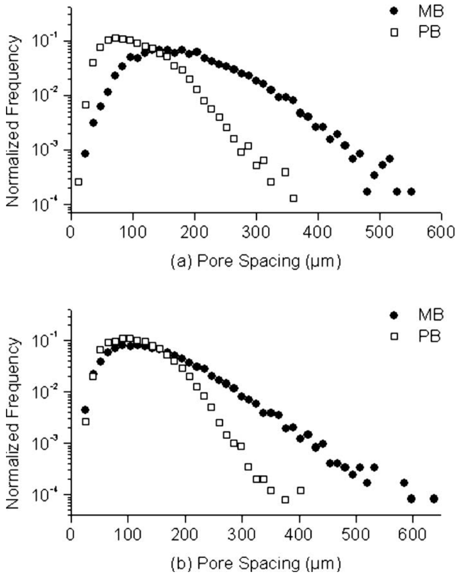

FIG. 12. Pore spacing distributions of (a) Fontainebleau and (b) Berea networks.

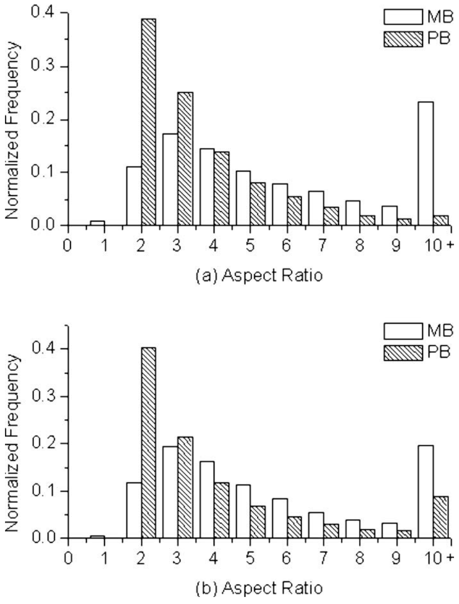

FIG. 13. Aspect ratio distributions of (a) Fontainebleau and (b) Berea networks.

We first compare the absolute permeabilities and formation factors of MB and PB networks for Fontainebleau and Berea sandstone; see Table II. Good agreement is found for both methods compared to calculations performed directly on the images. The absolute permeability of the MB network for Fontainebleau sandstone is closer to that calculated on the voxel image (345 mD) than for the PB network, although they are both low compared to 862 mD measured on a similar sample [41].

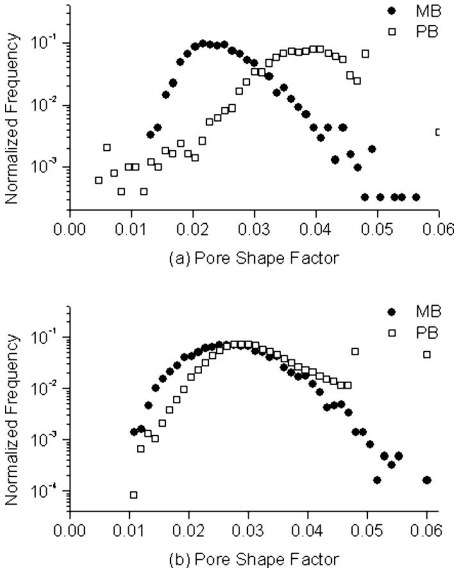

FIG. 14. Shape factor distributions of (a) Fontainebleau and (b) Berea networks.

TABLE II. Petrophysical properties of Fontainebleau and Berea networks.

	Fontainebleau network		Berea network	
Petrophysical properties	PB	MB	PB	MB
Net porosity	0.136	0.136	0.183	0.197
Clay bound porosity	0.0	0.0	0.057	0.07
Network permeability (mD)	582	380	2668	1111
Image permeability (mD)[a]	345		942	1286
Experimental permeability (mD)	862		1100	650
Network formation factor	34.93	30.57	14.33	14.58
Image formation factor[b]	51.0		36.9	24.1

[a] Image permeability is the absolute permeability calculated on image voxels using lattice Boltzmann simulation.

[b] Image formation factor is the formation factor calculated by solving Laplace equations on image voxels.

The two Berea networks have similar porosity but different absolute permeability. The absolute permeability of the PB network is 2668 mD compared to corresponding experimental value of 1100 mD [21]. The permeability of the MB network is 1111 mD compared to 650 mD measured on the core plug from which the imaged sample was taken and 1286 mD computed on the image. Again these results are consistent with the PB sample representing a slightly coarser-grained, more permeable sample. However, both networks overpredict experimental permeability. This may be due to the heterogeneity of the sample and the uncertainty associated in the course of imaging and image processing. Since the prediction made by the MB network is close to that calculated on the voxel image directly, the network extraction algorithm preserves permeability and that any errors are due to sample size and the image processing.

The results for the remaining samples are compared in Table III. The MB networks predict the absolute permeability successfully with an average overestimation factor of 1.11 compared to computations on the original images. However, the MB networks underestimate the formation factors by an average multiple of 1.73, which needs further investigation. Formation factor is the inverse of conductivity; hence we overestimate the conductivity of the system. Furthermore, the pore networks underestimate absolute permeability for some samples, such as carbonate sample C1 and a consolidated sandstone sample S4 due to uncertainties associated

TABLE III. Computed petrophysical properties of the samples studied.

Sample name	A1	S1	S2	S3	S4	S5	S6	S7	S8	S9	C1	C2	B.	F.	AVG
Rock type[a]	P	S	S	S	S	S	S	S	S	S	C	C	S	S	
Resolution (μm)	3.9	8.7	5.0	9.1	9.0	4.0	5.1	4.8	4.9	3.4	2.9	5.3	5.3	7.5	
Porosity (%)	42.9	14.1	24.6	16.9	17.1	21.1	24.0	25.1	34.0	22.2	23.3	16.8	19.6	13.5	
Average coordination number	6.67	3.15	4.77	3.32	2.72	3.32	4.0	5.23	5.94	3.32	3.0	2.37	3.98	3.85	
Kx (mD)[b]	8272	1969	4318	143	273	4638	11289	7268	13063	2735	785	38	1360	292	
Ky (mD)[b]	7977	1752	3983	420	289	4874	10683	7594	13507	2093	1469	161	1304	321	
Kz (mD)[b]	5412	1312	3394	109	215	4440	10951	6037	12936	1844	1053	18	1193	422	
Avg. K (mD)[b]	7220	1678	3898	224	259	4651	10974	6966	13169	2224	1102	72	1286	345	
Network K (mD)[b]	8076	1486	3950	281	169	5369	11282	7926	13932	3640	556	158	1111	380	
K overestimation factor[c]	1.12	0.89	1.01	1.25	0.65	1.15	1.03	1.14	1.06	1.64	0.50	2.18	0.86	1.10	1.11
FFx [b]	4.47	36.3	10.9	52.2	74.5	14.1	10.3	9.6	6.02	16.4	33.7	18	23.1	53.9	
FFy [b]	4.57	37.9	11.3	41.9	71.0	14.6	11.2	9.3	5.97	19.9	21.9	121	24.0	53.0	
FFz [b]	5.73	53.5	12.6	70.3	114.4	15.9	12.9	11.2	6.53	18.1	27.2	249	25.2	46.8	
Avg. FF[b]	4.86	41.3	11.5	52.4	82.8	14.8	11.4	9.9	6.16	18.0	26.8	170	24.1	51.0	
Network FF[b]	2.36	26.0	6.53	37.4	59.4	8.04	6.68	5.41	3.39	8.69	22.0	78.7	14.9	30.6	
FF underestimation factor[c]	2.06	1.59	1.77	1.40	1.39	1.84	1.70	1.84	1.82	2.07	1.22	2.16	1.65	1.67	1.73

[a] P=sandpack; S=sandstone; C=carbonate; B.=Berea sandstone (micro-CT image); F.=Fontainebleau sandstone (PB image).

[b] Kx, Ky, Kz, FFx, FFy, and FFz are the directional absolute permeability and formation factors in the x, y, and z directions, respectively; network K and FF are the absolute permeability and formation factors measured on the pore networks; Avg. K is the average absolute permeability; Avg. FF is the harmonic mean of the formation factors of the three directions.

[c] K overestimation factor is the ratio of network K to avg. K; FF underestimation factor is the ratio of avg. FF to network FF.

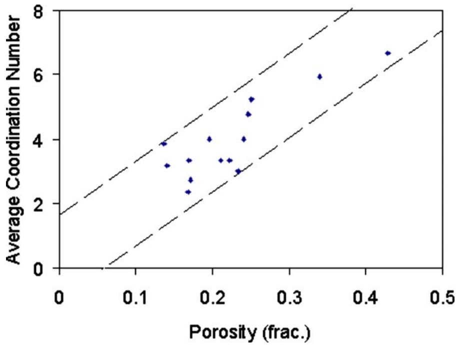

FIG. 15. (Color online) Average coordination number as a function of porosity for all the samples studied. The data embraced by the dash lines show a positive correlation.

with their insufficient image resolutions that may lead to the extraction of poorly connected networks.

Table III also gives the porosity and average coordination numbers of the studied rock samples. The samples cover a wide range of porosity from 0.13 to 0.43. Figure 15 reveals a trend that the average coordination number increases as the porosity increases. This explains the dependence of trapped nonwetting phase saturation on porosity proposed by Jerauld [47]. In his experiments, the maximum trapped gas saturation increased with decreased porosity because the reduced average coordination number indicates fewer paths available for gas to escape and trapping increases.

C. Multiphase flow properties

Primary drainage (oil flooding) and imbibition (water flooding) are simulated on both MB and PB networks for the two samples using the two phase code developed by Valvatne and Blunt [26]. For the Fontainebleau sandstone, the predicted relative permeability curves (Fig. 16) from the MB network are compared with those from the PB networks [20], while for Berea sandstone, the results (Figs. 17 and 18) from both MB and PB networks are compared to experimental data [42]; fluid properties input to the simulator are summarized in Table IV.

1. Fontainebleau sandstone

During primary drainage, the networks are assumed to be strongly water-wet with a receding contact angle of 0°. The similarity in the drainage relative permeability curves [Fig. 16(a)] indicates that the two networks are in good agreement in terms of topology and element geometry. The slightly less curving MB relative permeability may be consistent with a broader pore size distribution shown in Fig. 8.

To predict the water flood behavior, we assumed a uniform distribution of intrinsic contact angles between 50°–60° (the same range used by Valvatne and Blunt [26] to predict the properties of water-wet Berea sandstone). The two networks yield similar oil relative permeability and the same residual oil saturation [Fig. 16(b)]. The water relative permeability of MB network is higher than for the PB network. This is due to the smaller shape factors in the MB networks [Fig. 14(a)], which allows the wetting phase (water) to be better connected at the corners of the pores. While there is no direct experimental data to compare against, the very low water relative permeability for the PB network is unlikely to be correct.

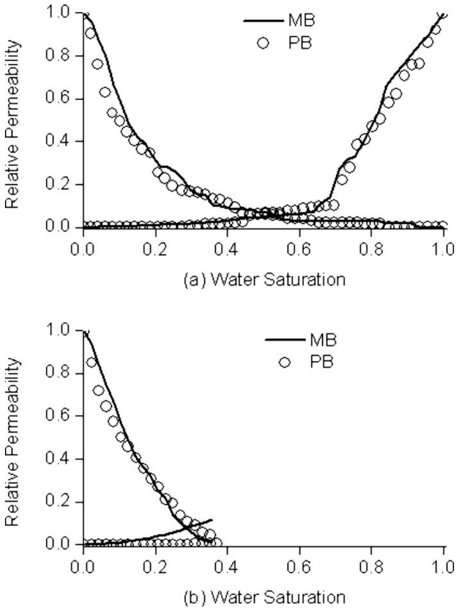

FIG. 16. Predicted (a) primary drainage and (b) water flooding relative permeability for water-wet reconstructed Fontainebleau sandstone using MB and PB networks.

2. Berea sandstone

Valvatne and Blunt [26] used a PB Berea pore network generated by Øren and Bakke [21] to predict the two-phase

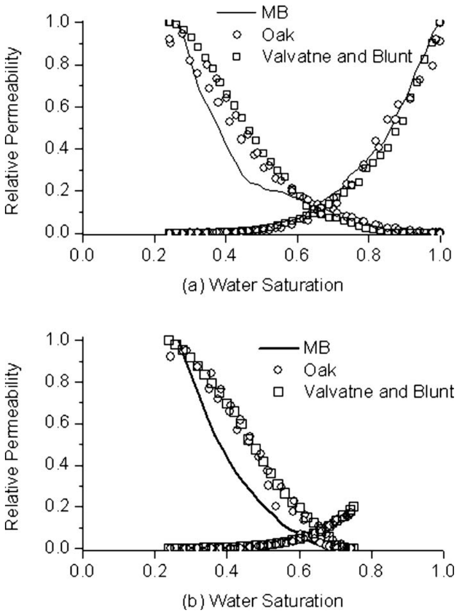

FIG. 17. Predicted (a) primary drainage and (b) water flooding relative permeabilities for water-wet Berea sandstone compared to Oak experimental data (sample 13 [42]) and Valvatne and Blunt's predictions [26].

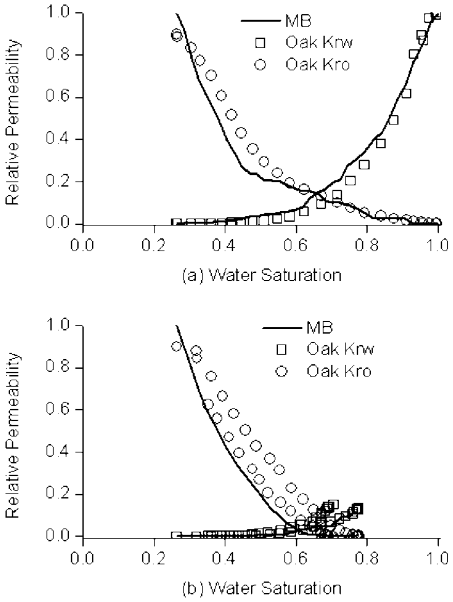

FIG. 18. Predicted (a) primary drainage and (b) water flooding relative permeabilities for water-wet Berea sandstone compared to experimental data (sample 14) by Oak [42].

behavior of water-wet Berea sandstone observed experimentally by Oak [42]. In the experiment, 1800 steady-state two-phase and three-phase relative permeability data had been collected using three fired Berea sandstone with different absolute permeabilities (sample 6: 200 mD; sample 13: 1000 mD; and sample 14: 800 mD). Valvatne and Blunt used sample 13 data for the predictions. The imaged sample in this work has a porosity of 22% and a permeability of 650 mD that is closer to sample 14. We use the extracted MB network to predict relative permeability for both samples. The fluid properties listed in Table IV were used by Oak in the experiments. We use the same properties for the simulation. The only input parameters we change for the predictions are the contact angles.

(a) Sample 13: Valvatne and Blunt used a receding contact angle of 0° for primary drainage and uniformly distributed the intrinsic contact angles between 50° and 60° for water flooding. In our simulation, we keep the same contact angle, 0, for primary drainage and uniformly distributed intrinsic contact angles between 50° to 70° to match the experimental residual oil saturation for water flooding. The predictions (Fig. 17) in general are in good agreement with both the experimental data and Valvatne and Blunt's prediction results. During primary drainage, the water relative permeability matches the experimental data very well. However, the oil relative permeability is low especially at the low water saturation end, which indicates that the larger elements in the network are poorly connected. This is consistent with the slightly lower average coordination number and the large number of poorly connected pores in the MB network. The water relative permeability during the water flooding again matches the experimental data well. However, the oil relative permeability is rather low compared to the experiment and PB network prediction. The lower shape factors and higher aspect ratios in the MB network allow more snap-off, or the filling of small throats by water, disconnecting the oil phase. However, since the primary drainage curve, when all the oil is connected, is lower, this is more likely to be due to underestimating the oil conductance. Other possibilities for the discrepancy include the dissimilarity in the original samples, the heterogeneity intrinsic to the samples, and the finite pore network size.

(b) Sample 14: we assign the same receding contact angles (0°) for primary drainage. For water flooding, the intrinsic contact angles are randomly chosen between $50°-75°$ to match the residual oil saturation. The relative permeability of primary drainage [Fig. 18(a)] is better predicted using sample 14 than sample 13, although the MB network predicts more curvature in the oil relative permeability indicating again poor connectivity of the oil phase. Low oil relative permeability is also seen for water flooding [Fig. 18(b)] indicating more snap-off trapping oil in the pores. On the other hand, the samples are not exactly the same and the network is rather small to present the whole core plug.

V. CONCLUSIONS

A maximal ball algorithm has been developed to extract pore networks from generic 3D images as the input to pore-scale models to predict single and multiphase flow in porous media. The extracted pore networks are compared to those extracted using a process-based method. Good agreement was obtained for both the structures of the networks and pore-scale transport predictions. A preliminary study on micro-CT imaging porous rocks has been performed on a series of sandstone, carbonate, and sand pack samples. A library of micro-CT images and relevant pore networks has been constructed. By studying this library, it is found that the MB pore networks yield good predictions of absolute permeability but underestimate the formation factors by an average of 70% compared to direct calculations on the voxel based images. The prediction of multiphase properties, such as relative permeability, is promising, although for Berea the

TABLE IV. Fluid properties used in the two-phase flow predictions.

Fluid properties	Fontainebleau sandstone	Berea sandstone sample 13	Berea sandstone sample 14
Surface tension (10^{-3} N/m)	30	30	30
Water viscosity (10^{-3} Pa/s)	1.05	1.05	1.05
Oil viscosity (10^{-3} Pa/s)	1.39	1.39	1.43

relative permeability of the oil phase is underestimated.

The current algorithm tends to find too many small throats especially when the image resolution is insufficient. The method finds throats by protruding ends of family trees to detect connectedness but cannot guarantee that every link is located at a hydraulic restriction. Further work is required to refine the method and improve predictions of single and multiphase flow properties.

ACKNOWLEDGMENTS

We would like to thank members of Imperial College Consortium on Pore-Scale Modeling and Numerical Rocks AS for supporting this project and providing data. We also thank Dr. Stefano Favretto and Professor Gianni Schena at Elettra Synchrotron for help with the micro-CT imaging.

[1] M. A. Celia, P. C. Reeves, and L. A. Ferrand, Rev. Geophys. **33**, 1049 (1995).

[2] M. J. Blunt, Curr. Opin. Colloid Interface Sci. **6**, 197 (2001).

[3] M. J. Blunt, M. D. Jackson, M. Piri, and P. H. Valvatne, Adv. Water Resour. **25**, 1069 (2002).

[4] J. Coenen, E. Tchouparova, and X. Jing, Proceedings of International Symposium of the Society of Core Analysts (www.sca-web.org).

[5] J. H. Dunsmuir, S. R. Ferguson, K. L. D'Amico, and J. P. Stokes, Proceedings of the 66th Annual Technical Conference and Exhibition of the Society of Petroleum Engineers, SPE 22860 (www.spe.org).

[6] P. M. Adler and J. F. Thovert, Appl. Mech. Rev. **51**, 537 (1998).

[7] S. Bekri, K. Xu, F. Yousefian, P. M. Adler, J. F. Thovert, J. Muller, K. Iden, A. Psyllos, A. K. Stubos, and M. A. Ioannidis, J. Pet. Sci. Eng. **25**, 107 (2000).

[8] M. A. Ioannidis and I. Chatzis, J. Colloid Interface Sci. **229**, 323 (2000).

[9] P. Levitz, Adv. Colloid Interface Sci. **76-77**, 71 (1998).

[10] Z. Liang, M. A. Ioannidis, and I. Chatzis, J. Colloid Interface Sci. **221**, 13 (2000).

[11] J. A. Quiblier, J. Colloid Interface Sci. **98**, 84 (1984).

[12] A. P. Roberts and S. Torquato, Phys. Rev. E **59**, 4953 (1999).

[13] C. L. Yeong and S. Torquato, Phys. Rev. E **57**, 495 (1998).

[14] C. L. Yeong and S. Torquato, Phys. Rev. E **58**, 224 (1998).

[15] H. Okabe and M. J. Blunt, Phys. Rev. E **70**, 066135 (2004).

[16] K. Wu, N. Nunan, J. W. Crawford, I. M. Young, and K. Ritz, Soil Sci. Soc. Am. J. **68**, 346 (2004).

[17] S. L. Bryant and M. J. Blunt, Phys. Rev. A **46**, 2004 (1992).

[18] S. L. Bryant, P. R. King, and D. W. Mellor, Transp. Porous Media **11**, 53 (1993).

[19] S. L. Bryant, D. W. Mellor, and C. A. Cade, AIChE J. **39**, 387 (1993).

[20] P.-E. Øren and S. Bakke, Transp. Porous Media **46**, 311 (2002).

[21] P.-E. Øren and S. Bakke, J. Pet. Sci. Eng. **39**, 177 (2003).

[22] S. Bakke and P.-E. Øren, SPEJ **2**, 136 (1997).

[23] S. Chen and G. D. Doolen, Annu. Rev. Fluid Mech. **30**, 329 (1998).

[24] C. Manwart, U. Aaltosalmi, A. Koponen, R. Hilfer, and J. Timonen, Phys. Rev. E **66**, 016702 (2002).

[25] T. W. Patzek, SPEJ **6**, 144 (2001).

[26] P. H. Valvatne and M. J. Blunt, Water Resour. Res. **40**, W07406 (2004).

[27] M. Piri and M. J. Blunt, Phys. Rev. E **71**, 026301 (2005).

[28] M. Piri and M. J. Blunt, Phys. Rev. E **71**, 026302 (2005).

[29] C. A. Baldwin, A. J. Sederman, M. D. Mantle, P. Alexander, and L. F. Gladden, J. Colloid Interface Sci. **181**, 79 (1996).

[30] Z. R. Liang, C. P. Fernandes, F. S. Magnani, and P. C. Philippi, J. Pet. Sci. Eng. **21**, 273 (1998).

[31] W. B. Lindquist, S. M. Lee, D. Coker, K. Jones, and P. Spanne, J. Geophys. Res. **101** (B4), 8297 (1996).

[32] W. B. Lindquist and A. Venkatarangan, Phys. Chem. Earth, Part A Solid Earth Geod. **24**, 593 (1999).

[33] A. P. Sheppard, R. M. Sok, and H. Averdunk, Proceedings of International Symposium of the Society of Core Analysts (www.sca-web.org).

[34] M. Prodanović, W. B. Lindquist, and R. S. Seright, J. Colloid Interface Sci. **298**, 282 (2006).

[35] Z. Jiang, K. Wu, G. Couples, M. I. J. van Dijke, K. S. Sorbie, and J. Ma, Water Resour. Res. **43**, W12S03 (2007).

[36] H. Shin, W. B. Lindquist, D. L. Sahagian, and S. R. Song, Comput. Geosci. **31**, 473 (2005).

[37] A. S. Al-Kharusi and M. J. Blunt, J. Pet. Sci. Eng. **56**, 219 (2007).

[38] D. B. Silin, G. Jin, and T. W. Patzek, Proceedings of the SPE Annual Technical Conference and Exhibition, SPE 84296 (www.spe.org).

[39] D. Silin and T. Patzek, Physica A **371**, 336 (2006).

[40] G. Mason and N. R. Morrow, J. Colloid Interface Sci. **141**, 262 (1991).

[41] T. Bourbie and B. J. Zinszner, J. Geophys. Res. **90**, 11524 (1985).

[42] M. J. Oak, Proceedings of the SPE/DOE Seventh Symposium on Enhanced Oil Recovery, Society of Petroleum Engineers, SPE 20183 (www.spe.org).

[43] P. L. Churcher, P. R. French, J. C. Shaw, and L. L. Schramm, Proceedings of the SPE International Symposium on Oilfiled Chemistry, SPE 21044 (www.spe.org).

[44] F. A. L. Dullien, *Porous Media: Fluid Transport and Pore Structure*, 2nd ed. (Academic, San Diego, 1992).

[45] See EPAPS Document No. E-PLEEE8-80-220908 for pictures of cross sections, extracted networks, and structural statistics of all the rock samples in this study. For more information on EPAPS, see http://www.aip.org/pubservs/epaps.html.

[46] N. C. Gallagher and G. L. Wise, IEEE Trans. Acoust., Speech, Signal Process. **29**, 1136 (1981).

[47] G. R. Jerauld, SPERE **12**, 66 (1997).